Path induced coherent energy transfer in light-harvesting complexes in purple bacteria

Sun, Kewei; Ye, Jun; Zhao, Yang

2014

Sun, K., Ye, J., & Zhao, Y. (2014). Path induced coherent energy transfer in light-harvesting complexes in purple bacteria. The journal of chemical physics, 141(12).

https://hdl.handle.net/10356/100198

https://doi.org/10.1063/1.4895791

Path induced coherent energy transfer in light-harvesting complexes in purple bacteria

Kewei Sun, Jun Ye, and Yang Zhao

Citation: The Journal of Chemical Physics **141**, 124103 (2014); doi: 10.1063/1.4895791
View online: http://dx.doi.org/10.1063/1.4895791
View Table of Contents: http://scitation.aip.org/content/aip/journal/jcp/141/12?ver=pdfcov
Published by the AIP Publishing

Path induced coherent energy transfer in light-harvesting complexes in purple bacteria

Kewei Sun,[1,2] Jun Ye,[1] and Yang Zhao[1,a)]
[1]*Division of Materials Science, Nanyang Technological University, Singapore 639798*
[2]*School of Science, Hangzhou Dianzi University, Hangzhou 310018, China*

(Received 3 July 2014; accepted 4 September 2014; published online 22 September 2014)

Features of path dependent energy transfer in a dual-ring light-harvesting (LH2) complexes (B850) system have been examined in detail systematically. The Frenkel-Dirac time dependent variational method with the Davydov D_1 Ansatz is employed with detailed evolution of polaron dynamics in real space readily obtained. It is found that the phase of the transmission amplitude through the LH2 complexes plays an important role in constructing the coherent excitonic energy transfer. It is also found that the symmetry breaking caused by the dimerization of bacteriochlorophylls and coherence or correlation between two rings will be conducive in enhancing the exciton transfer efficiency. © *2014 AIP Publishing LLC*. [http://dx.doi.org/10.1063/1.4895791]

I. INTRODUCTION

As an essential photochemical process in plants and bacteria, photosynthesis plays the central role in net primary production on earth by converting carbon dioxide into organic compounds. In photosynthetic purple bacteria the antenna complexes function as light-harvesting systems that absorb light radiation and transfer the excitation energy to specialized pigment-protein complexes (PPCs) or the reaction centers (RCs). Antenna complexes have a highly symmetric multi-ring structure.[1,2] The peripheral antenna complex known as the light harvesting (LH2) complex of purple bacteria is a dual-ring circular aggregate built from eight, nine, or ten units of $\alpha\beta$-heterodimers forming C8, C9, or C10 symmetry, respectively. Each unit contains a pair of α and β apoproteins, three bacteriochlorophyll-a (Bchl-a) molecules, and a carotenoid, such that the Bchl-a molecules form two rings, which are named as B800 and B850 rings, according to their respective absorption maxima at 800 nm and 850 nm. The B850 ring in the photosynthetic apparatus of *Rhodospirillum molischianum* consists of 16 tightly positioned BChls-a, with Mg-Mg distance of about 9.36 Å within $\alpha\beta$-heterodimers, which in turn, are separated by about 8.78 Å.[3]

It is found that the excitation energy from photoexcitation is transferred with a high efficiency (>95%) to specialized PPCs or the RCs.[4–6] The relevant experiments probing excitonic transport in green sulphur bacteria suggest that quantum coherence is an essential phenomenon in photosynthesis,[7–9] a process in which electronic excitations generated by solar photons exhibit wave-like behavior before being trapped at particular pigment sites. Study of quantum coherence is facilitated by the ease to observe electronic superpositions and their evolution using 2D electronic spectroscopy techniques.[7,8,10,11] Very recently, it has been observed that phase control of the quantum interference between the excitation pathways to B800 and B850 excited states alters the excitation probability[12,13] in the pump-probe experiment. The electronic coherence has been argued to survive for a relatively long time (about several hundred femtoseconds) despite the decoherence effects induced by the environment. It is suggested that quantum coherence might play a significant role in achieving the remarkably high efficiency.[3,6,14–30] In addition, quantum coherence may be easily destroyed by strong environmental coupling. On the other hand, slow and spatially correlated fluctuations of the protein environment may be responsible to provide sustained quantum coherence for excitation dynamics, an effect known as environmentally assisted quantum transport (ENAQT).[25–27,31] In other words, the protein environment plays the dual role of simultaneously destroying and preserving excitonic coherence. An overall effect of the complicated interactions between the exciton and its environment facilitates coherent energy transfer. Whether coherent quantum dynamics is a critical component in determining highly efficient energy transfer in large systems or not, remains a debated question till date.[32] These exciting findings have inspired designs of efficient artificial systems that can direct, sort, and respond to excitation energy in sophisticated manners.[32]

Traditional theories, such as the Förster resonance energy transfer (FRET) approach based on the weak-coupling approximation and the Redfield equation method based on the Markovian approximation, have been applied to study the energy transfer processes in the photosynthetic complexes.[33–36] The classical Förster theory treats electronic coupling perturbatively and also assumes incoherent donor-acceptor hopping induced by dipolar interactions between chromophores.[37] The often employed assumption of point dipoles is, however, inadequate in describing pigment aggregation.[38] On the other hand, the Redfield equation is only applicable in the limit of weak exciton-phonon coupling. Therefore, these methods suffer from a variety of deficiencies and cannot be applied to a realistic photosynthetic system with an intermediate coupling strength. Recently, sophisticated theoretical methods such as the multichromophoric FRET theory (MC-FRET), and the

a)Electronic mail: YZhao@ntu.edu.sg

hierarchical equation of motion (HEOM) approach have been employed to study the mechanisms behind these highly efficient photosynthetic processes.[18–20] The MC-FRET theory can be applied to cope with the transfer pathway interference that is not accounted for in earlier single-chromophore FRET treatments, but when the electronic coupling is strong but the system-bath coupling is weak, it is necessary to consider relaxation of delocalized exciton states. For the HEOM approach, it is commonly assumed that phonon degrees of freedom are at thermal equilibrium, an assumption that may not be fulfilled when dealing with fast exciton dynamics (hundreds of fs) and strong exciton-phonon coupling.

To gain a detailed understanding of the intra- or inter-ring excitonic energy transfer (EET) processes, we adopt the Frenkel-Dirac time-dependent variational method to study quantum dynamics of the Holstein polaron via the Davydov D_1 Ansatz with a reliable accuracy.[39–41] Interesting and important physical mechanisms such as transmission phase, constructive/destructive interference, mechanism of exciton delocalization or localization, and "speed up" of the energy transfer by quantum coherence, are captured by the time-dependent variational method, shedding light on path induced coherent energy transfer in LH2 complexes.

The rest of the paper is organized as follows. In Sec. II, we introduce formalisms accounting for quantum dynamics of excitonic energy transfer in coupled ring systems. Polaron dynamics of various model systems as well as effects of dimerization have been discussed in detail in Sec. III. Finally, conclusions are drawn in Sec. IV.

II. METHODOLOGY

The energy transfer process in the light-harvesting apparatus of the purple bacteria can be usually described as one taking place in a one-dimensional exciton-phonon system, namely, the Holstein model. The Holstein Hamiltonian for an exciton-phonon system is given by[42,43]

$$\hat{H} = \hat{H}_{\rm ex} + \hat{H}_{\rm ph} + \hat{H}_{\rm ex-ph}, \tag{1}$$

where $\hat{H}_{\rm ex}$ is the Frenkel-exciton Hamiltonian, $\hat{H}_{\rm ph}$ represents the phonon Hamiltonian, and $\hat{H}_{\rm ex-ph}$ is the exciton-phonon interaction part. To account for excitonically coupled multiple-ring system, each term of the original Holstein Hamiltonian can be expressed as

$$\hat{H}_{\rm ex} = \sum_{r_1 \neq r_2} \sum_{nm} J_{nm}^{r_1 r_2} \hat{a}_n^{r_1 \dagger} \hat{a}_m^{r_2} + \sum_r \sum_{nm} J_{nm}^r \hat{a}_n^{r\dagger} \hat{a}_m^r, \tag{2}$$

$$\hat{H}_{\rm ph} = \sum_r \sum_q \omega_q^r \hat{b}_q^{r\dagger} \hat{b}_q^r, \tag{3}$$

$$\hat{H}_{\rm ex-ph} = -\frac{1}{\sqrt{N}} \sum_r \sum_n \sum_q g_q^r \omega_q^r \hat{a}_n^{r\dagger} \hat{a}_n^r \left(e^{iqn} \hat{b}_q^r + H.c. \right), \tag{4}$$

where $H.C.$ stands for Hermitian conjugate, $\hat{a}_n^{r\dagger}$ ($\hat{a}_n^r$) is the creation (annihilation) operator for an exciton at the nth site (for the B850 ring, the total number of sites is equal to 16 for each ring) of the rth ring (with total number of $N_{\rm ring}$ rings), $J_{nm}^{r_1 r_2}$ is the exciton transfer integral between two sites of different rings, and J_{nm}^r is the Frenkel exciton Hamiltonian for the rth ring[44]

$$J_{nm}^r = \begin{pmatrix} \varepsilon_1 & J_1 & W_{1,3} & \cdot & \cdot & \cdot & J_2 \\ J_1 & \varepsilon_2 & J_2 & \cdot & \cdot & \cdot & W_{2,2N} \\ W_{3,1} & J_2 & \varepsilon_1 & \cdot & \cdot & \cdot & \cdot \\ \cdot & \cdot & \cdot & \cdot & \cdot & \cdot & \cdot \\ \cdot & \cdot & \cdot & \cdot & \varepsilon_2 & J_2 & W_{2N-2,2N} \\ \cdot & \cdot & \cdot & \cdot & J_2 & \varepsilon_1 & J_1 \\ J_2 & \cdot & \cdot & \cdot & W_{2N,2N-2} & J_1 & \varepsilon_2 \end{pmatrix}. \tag{5}$$

In the above equation, ε_1 and ε_2 are the on-site excitation energies of an individual BChl-a. J_1 and J_2 are the transfer integrals between nearest neighbors, N equals to 8 as the system is of C8 symmetry, and matrix elements $W_{i,j}$ are dipolar coupling strengths for the non-nearest neighbors. We first discuss the case with no diagonal disorder, and for simplicity, the site energy is set as zero. Later in Sec. III, we will introduce a form of diagonal disorder ($\delta\varepsilon_n$) obeying the Gaussian distribution. In Eq. (5), dipolar coupling between site i and site j takes the form

$$W_{i,j} = C \left[\frac{\mathbf{d}_i \cdot \mathbf{d}_j}{|\mathbf{r}_{ij}|^3} - \frac{3(\mathbf{d}_i \cdot \mathbf{r}_{ij})(\mathbf{d}_j \cdot \mathbf{r}_{ij})}{|\mathbf{r}_{ij}|^5} \right], \tag{6}$$

where C is the proportionality constant, $\mathbf{r}_{ij}$ is the vector connecting the ith and jth monomers, and $\mathbf{d}_i$ are the unit vectors of the ith BChl-a. The following parameters are adopted:[3] $J_1 = 594\,{\rm cm}^{-1}$, $J_2 = 491\,{\rm cm}^{-1}$, and $C = 640725\,{\rm Å}^3\,{\rm cm}^{-1}$. $\hat{b}_q^{r\dagger}$ ($\hat{b}_q^r$) is the creation (annihilation) operator of a phonon with momentum $q = 2\pi n_q/16$ ($n_q = -7, -6, \cdots, 7, 8$) and frequency ω_q^r in the $r^{\rm th}$ ring, and the Planck constant is set as $\hbar = 1$. $\hat{H}_{\rm ex-ph}$ is the linear, diagonal exciton-phonon coupling Hamiltonian with the coupling constant $g_q^r = g$. The Huang-Rhys factor S can be obtained from $\sum_q g_q^{r2} \omega_q^r = S\omega_0$, where $\omega_0 = 1670\,{\rm cm}^{-1}$ is the characteristic phonon frequency.[45] For simplicity, ω_0 is set to one energy unit in this work. Therefore, all other energy quantities are scaled by the characteristic phonon frequency. $S = 0.5$ is used in the calculations.

The exciton dynamics in a dual-ring LH2 system is studied using the Davydov D_1 Ansatz and the Lagrangian formalism of the Dirac-Frenkel time-dependent variational method.[39,40,46] It is easy to extend our method to multiple-ring system without too much additional computational expenses. The dual-ring system is initialized as follows: $\alpha_n^r(0) = \delta_{r,1}\delta_{n,9}$ and $\lambda_{n,q}^r(0) = 0$. A linear dispersion phonon with a bandwidth $W = 0.8$ is assumed in our calculation. The reader is referred to the Appendix for detailed derivations of the equations of motion for the variational parameters.

III. RESULTS AND DISCUSSIONS

A series of consistent model studies of coupled LH2 complexes separated by a tip-to-tip distance of 15 Å will be presented in this section. According to the exciton Hamiltonian (5), there are substantial inter-ring dipolar interactions between sites 1, 2, and 16 of ring-1 and sites 8, 9, and 10 of ring-2, which dominate the inter-ring excitonic transfer.

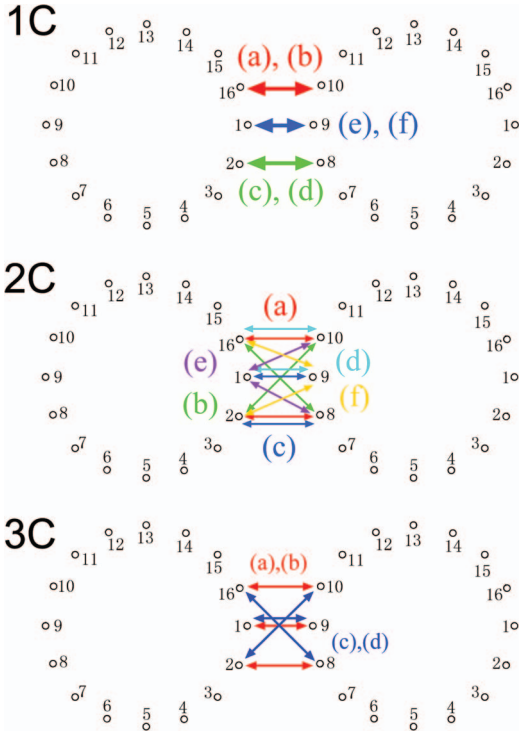

FIG. 1. Schematics of the exciton transfer pathways with various numbers of channels. Here 1C, 2C, and 3C represent pathways with 1, 2, and 3 channels, respectively. In 1C pathways, (a), (c), (e) denote cases with $J_1 = J_2$ and (b), (d), (f) denote cases with $J_1 \neq J_2$. In 2C pathways, each label corresponds to one type of channel combination with either $J_1 = J_2$ or $J_1 \neq J_2$. In 3C pathways, (a) and (c) correspond to cases with $J_1 = J_2$ while (b) and (d) denote cases with $J_1 \neq J_2$.

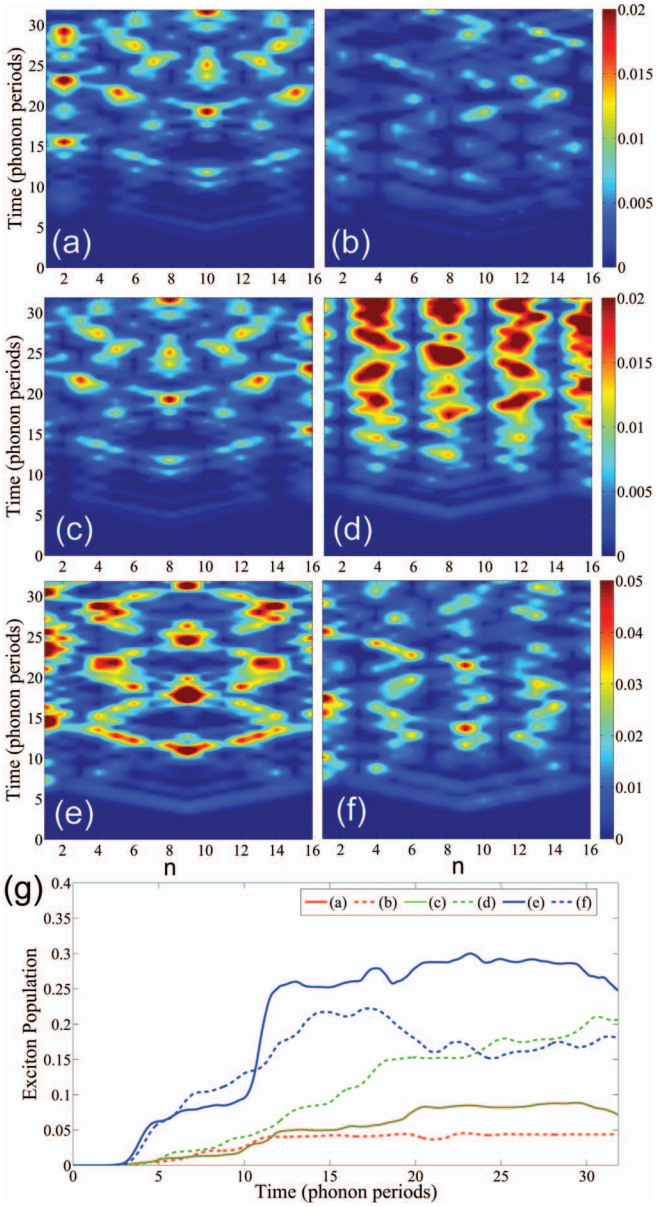

FIG. 2. Real space dynamics of exciton probability $|\alpha_n(t)|^2$ of ring-2. (a) $J_1 = J_2 = 0.3557$ with a channel: ring-1(16)↔ring-2(10). (b) $J_1 = 0.3557$ and $J_2 = 0.2940$ with a channel: ring-1(16)↔ring-2(10). (c) $J_1 = J_2 = 0.3557$ with a channel: ring-1(2)↔ring-2(8). (d) $J_1 = 0.3557$ and $J_2 = 0.2940$ with a channel: ring-1(2)↔ring-2(8). (e) $J_1 = J_2 = 0.3557$ with a channel: ring-1(1)↔ring-2(9). (f) $J_1 = 0.3557$ and $J_2 = 0.2940$ with a channel: ring-1(1)↔ring-2(9). (g) The population of ring-2 as a function of time for all of the above cases. Channel configurations for the transfer pathways of this type can be found in pathways 1C shown in Fig. 1.

As a result, there emerge various possible pathways or channels for inter-ring EET to take place. Dependance of polaron dynamics and EET efficiency on energy transfer channels is then investigated along selected combinations of transfer pathways. To facilitate further discussions, we define a notation for a transfer channel, e.g., ring-1(16)↔ring-2(10) describes a channel linking site 16 of ring-1 and site 10 of ring-2. To avoid possible interference of the non-nearest neighbor intra-ring dipolar interactions, only J_1 and J_2 are considered for each ring. Moreover, a single excitation is created initially on site 9 of ring-1 for all the cases.

A. Effects of exciton transfer pathways

Selected exciton transfer pathways between the two LH2 rings are illustrated in Fig. 1 and can be divided into three different types, 1C, 2C, and 3C, corresponding to one, two, and three exciton transfer channels, respectively. For example, the 2C type in Fig. 1 includes 6 subtypes, and 2C (a) labels a two-channel transfer: ring-1(2)↔ring-2(8) and ring-1(16)↔ring-2(10). For all the transfer pathways types, cases with $J_1 = J_2$ and $J_1 \neq J_2$ have been studied systematically.

For simplicity, the pathways with single transfer channel from ring-1 to ring-2 are studied first. Figs. 2(a), 2(c), and 2(e) depict the real space dynamics of exciton along ring-1(16)↔ring-2(10), ring-1(2)↔ring-2(8), and ring-1(1)↔ring-2(9), respectively, for the case of $J_1 = J_2 = 0.3557$. On the other hand, Figs. 2(b), 2(d), and 2(f) correspond to the same three cases with $J_1 = 0.3557$ and $J_2 = 0.2940$. Fig. 2(a) is fully equivalent to Fig. 2(c) due to translational symmetry of the transfer channels, a fact which is also reflected in Fig. 2(g) showing the corresponding equivalent population in ring 2. However, if one compares Fig. 2(b) to Fig. 2(d), different excitonic dynamics evolution is observed, which can be simply explained as a result of symmetry breaking caused by dimerization of BChls, i.e., $J_1 \neq J_2$. In fact, it is revealed in Fig. 2(g) that the exciton population corresponding to Fig. 2(d) is greater than that corresponding to Fig. 2(b).

Focusing on Figs. 2(c) and 2(d), it is found that the exciton exhibits localized characteristics within a certain dimer block. Comparing other figures with $J_1 = J_2$ to those with $J_1 \neq J_2$, this feature appears to be universally true for all cases with $J_1 \neq J_2$, suggesting a critical role of dimerization. In addition, it is found that the dimerization exerts has different influence (positive or negative) on the efficiency of the population transfer for different pathways.

Channel ring-1(1)↔ring-2(9) has the maximum transfer rate owing to its relatively small transfer length and thus the strongest inter-ring coupling. As a result, greater populations are also observed in corresponding Figs. 2(e) and 2(f). For all the uniform dipolar coupling cases (with $J_1 = J_2$) shown in Figs. 2(a), 2(c), and 2(e), typical single-site dynamics with well-resolved wavefronts is obtained. The wavefronts of the exciton on site 9 initially move along two opposite directions in ring-1, before reaching the transfer channel. For ring-1(1)↔ring-2(9) channel, the two wavefronts preserve the same phase and are then transferred to ring-2. More importantly, coherent enhancement is observed in ring-2. Such enhancement can be explained as constructive interference appearing at the incidence sites of ring-2 and at their diametrically opposite sites, with a phase difference of π. This interesting interference phenomenon stems from the phase of transmission resulting via the channel transfer and intra-ring transfer. The physical paradigm mentioned above also remains applicable to the dynamics of LH2 rings with realistic exciton Hamiltonian. However, for a realistic LH2 exciton Hamiltonian, the role of structural dimerization needs to be taken into account, which may lead to different features in the exciton evolution dynamics.

To gain in-depth understanding into the coherence and inter-ring exciton transfer, we constructed models with multiple transfer channels. Calculations have been performed for the cases with dual-channel and triple-channel pathways to represent realistic scenarios as much as possible. Fig. 3 illustrates the real space dynamics in the dual-channel cases, with uniform ($J_1 = J_2 = 0.3557$) dipolar coupling. Interestingly, Fig. 3(a) exhibits constructive interference at site 1 and 9 of ring-2. Excitonic wavefronts that transfer through two pathways, i.e., ring-1(16)↔ring-2(10) and ring-1(2)↔ring-2(8), lead to the first interference at site 9 of ring-2. Due to the phase difference between exciton wavefronts propagating through the pathways corresponding to Figs. 3(c) and 3(d), the exciton population in ring-2 (see Fig. 3(c) or Fig. 3(d)) is close to or smaller than that of the single channel case (see Fig. 2(e)). The phase difference between the two wavefronts caused by the total intra- and inter-ring pathlengths is a basic factor which decides the efficiency of excitonic population transfer. A general conclusion about smaller population can be arrived at for the dual-channel cases by comparing Figs. 2(g) and 3(g). These findings suggest that the nature of transfer channels and intra-ring transfer patterns play prominent roles in determining constructive or bright regions in the quantum interference within each ring. In addition, there is also a mirror symmetry between Figs. 3(c) and 3(d) due to the topological equivalence of the dual-channel transfer. Due to the unfavorable phase difference and extremely small inter-ring coupling for the channels corresponding to Figs. 3(e) and 3(f), the exciton populations become so small that we neglect their contributions.

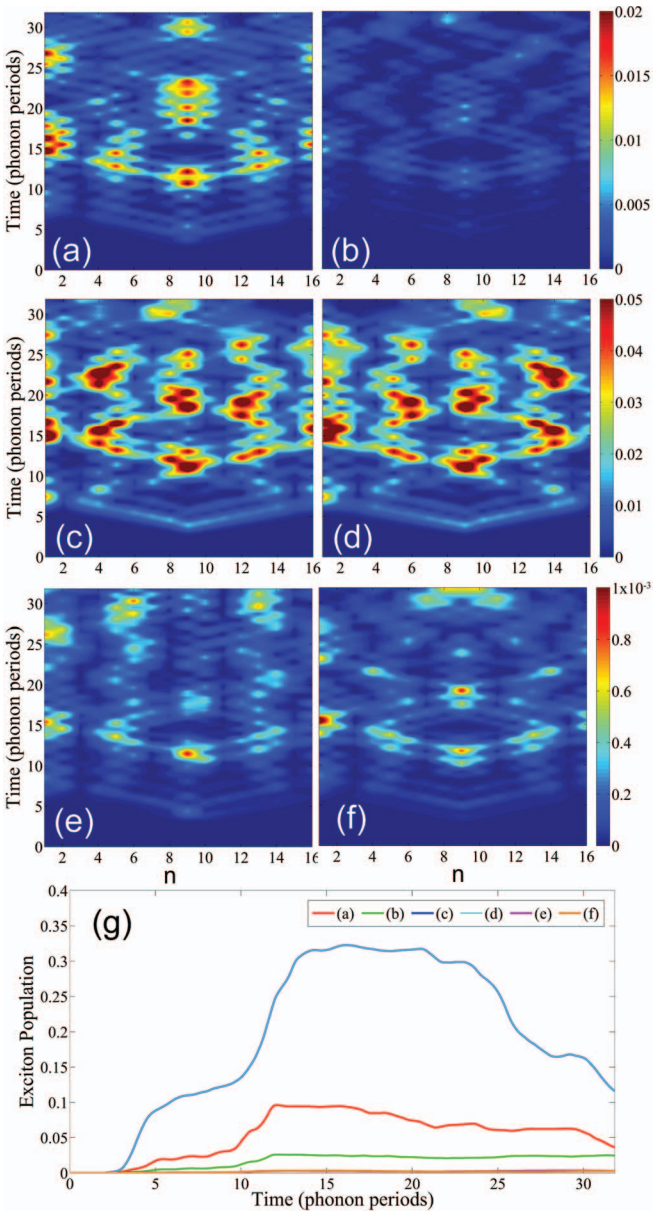

FIG. 3. Real space dynamics of exciton probability $|\alpha_n(t)|^2$ of ring-2 with $J_1 = J_2 = 0.3557$. (a) Dual-channel: ring-1(16)↔ring-2(10) and ring-1(2)↔ring-2(8). (b) Dual-channel: ring-1(16)↔ring-2(8) and ring-1(2)↔ring-2(10). (c) Dual-channel: ring-1(2)↔ring-2(8) and ring-1(1)↔ring-2(9). (d) Dual-channel: ring-1(16)↔ring-2(10) and ring-1(1)↔ring-2(9). (e) Dual-channel: ring-1(1)↔ring-2(10) and ring-1(1)↔ring-2(8). (f) Dual-channel: ring-1(2)↔ring-2(9) and ring-1(16)↔ring-2(9). (g) The population of ring-2 as a function of time for all of the above cases. Channel configurations for the transfer pathways of this type can be found in pathways 2C shown in Fig. 1.

Further, we investigate the effects of non-uniform dipolar coupling in the dual-channel cases. The real space dynamics of exciton and population of ring-2 are depicted in Fig. 4 with $J_1 = 0.3557$ and $J_2 = 0.2940$, while all other conditions are same as Fig. 3. An evident enhancement of exciton population can be readily noted by comparing Figs. 4(a) and 4(b) with Figs. 3(a) and 3(b) owing possibly to the constructive interference. Figs. 4(c) and 4(d) exhibit different exciton evolution

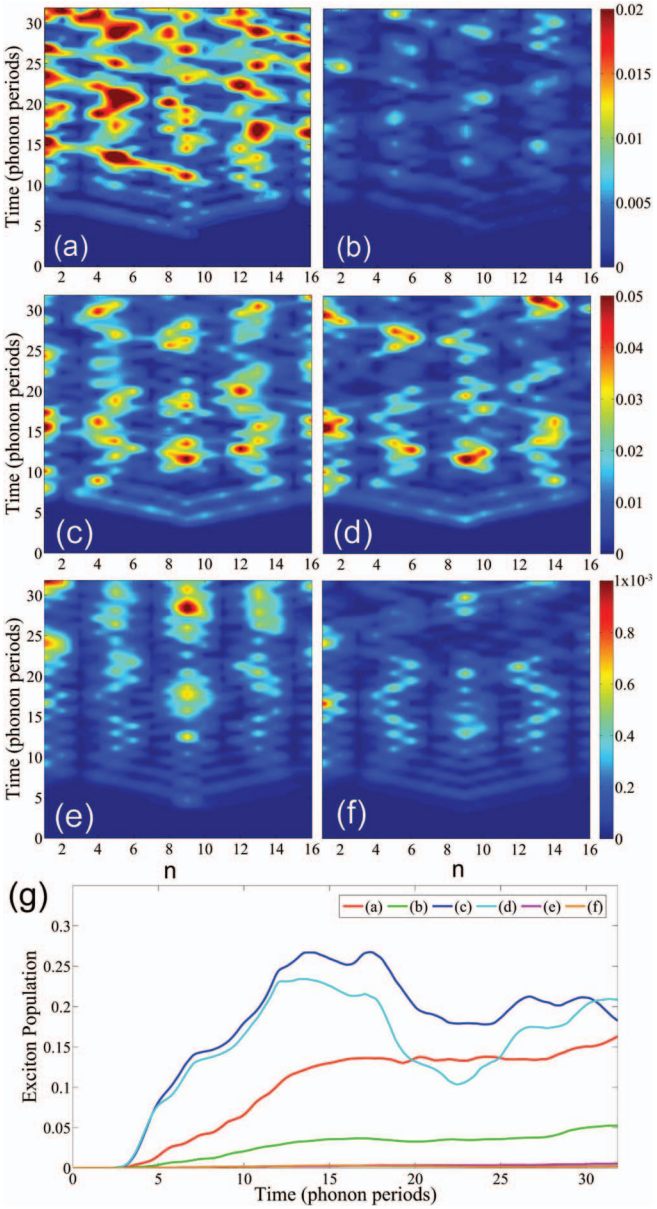

FIG. 4. Real space dynamics of exciton probability $|\alpha_n(t)|^2$ of ring-2 with $J_1 = 0.3557$ and $J_2 = 0.2940$. (a) Dual-channel: ring-1(16)↔ring-2(10) and ring-1(2)↔ring-2(8). (b) Dual-channel: ring-1(16)↔ring-2(8) and ring-1(2)↔ring-2(10). (c) Dual-channel: ring-1(2)↔ring-2(8) and ring-1(1)↔ring-2(9). (d) Dual-channel: ring-1(16)↔ring-2(10) and ring-1(1)↔ring-2(9). (e) Dual-channel: ring-1(1)↔ring-2(10) and ring-1(1)↔ring-2(8). (f) Dual-channel: ring-1(2)↔ring-2(9) and ring-1(16)↔ring-2(9). (g) The population of ring-2 as a function of time for all of the above cases. Channel configuration for the transfer path of this type can be found in pathways 2C shown in Fig. 1.

dynamics since the symmetry between Figs. 3(c) and 3(d) is destroyed by the dimerization, which is also easy to be identified in Fig. 4(g). In addition, Figs. 4(e) and 4(f) still show a very low population transfer efficiency. The contributions of these two cases are minor. In the presence of dimerization effects, the localization characteristics are observed to prevail, as shown in all the dual-channel cases.

Finally, we study the EET characteristics along three-channel pathways with the uniform coupling case and the dimerization case, as shown in Fig. 5. We expect this

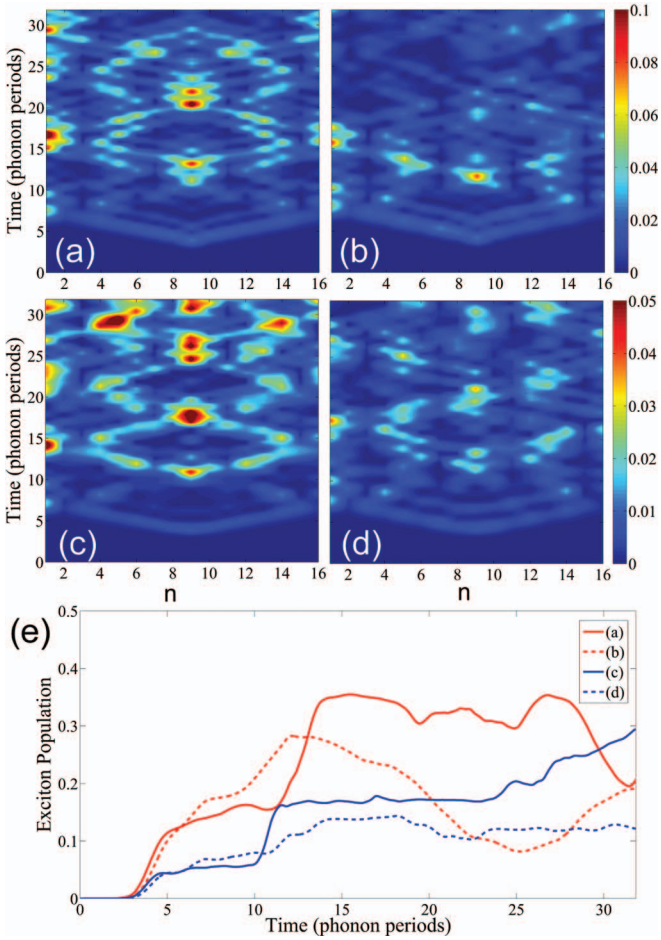

FIG. 5. Real space dynamics of exciton probability $|\alpha_n(t)|^2$ in ring-2. (a) $J_1 = J_2 = 0.3557$ with three-channel: ring-1(16)↔ring-2(10), ring-1(1)↔ring-2(9), and ring-1(2)↔ring-2(8). (b) $J_1 = 0.3557$ and $J_2 = 0.2940$ with three-channel: ring-1(16)↔ring-2(10), ring-1(1)↔ring-2(9), and ring-1(2)↔ring-2(8). (c) $J_1 = J_2 = 0.3557$ with three-channel: ring-1(16)↔ring-2(8), ring-1(1)↔ring-2(9), and ring-1(2)↔ring-2(10). (d) $J_1 = 0.3557$ and $J_2 = 0.2940$ with three-channel: ring-1(16)↔ring-2(8), ring-1(1)↔ring-2(9), and ring-1(2)↔ring-2(10). (e) The population of ring-2 as a function of time for all of the above cases. Channel configuration for the transfer path of this type can be found in pathways 3C shown in Fig. 1.

particular model to closely resemble the real-life system. Figs. 5(a) and 5(c) exhibit similar dynamical behaviors as that in Fig. 2(e). While the dominant contribution to EET comes from the channel ring-1(1)↔ring-2(9), the dimerization exerts a negative impact on the EET efficiency in this case. Impressively, the dimerization can improve the average efficiency of the population transfer during the first 10 phonon periods. This observation holds true for all the cases with $J_1 \neq J_2$. In the light of all the aforementioned findings, it can be argued that the EET process depends significantly on the specific channel and thus the symmetry. An efficient EET transfer pathway in terms of population transfer inevitably requires involvement of a channel with sufficiently strong exciton coupling, such as the channel ring-1(1)↔ring-2(9).

B. Effects of static disorder

In order to investigate the effects of the coherence on the EET efficiency, we introduce diagonal disorder with a

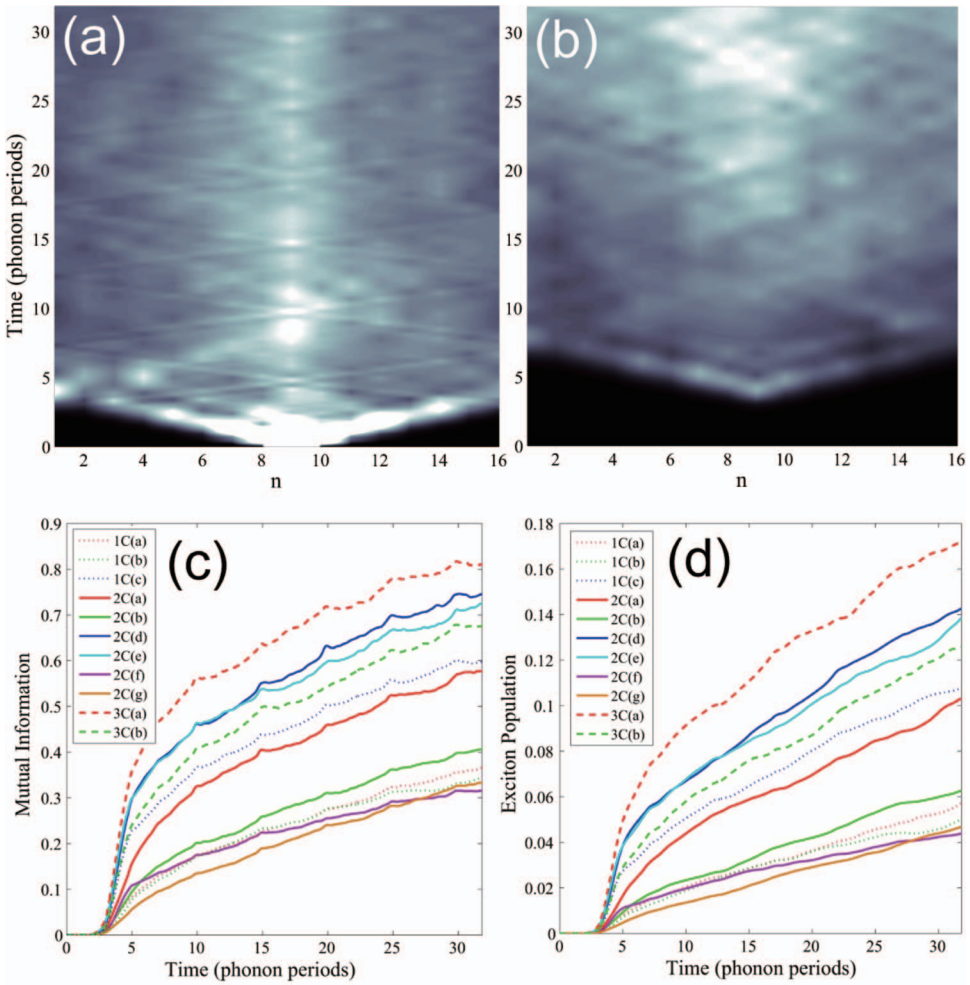

FIG. 6. Effects of static disorder on the real space dynamics of exciton probability $|\alpha_n(t)|^2$ in (a) ring-1 and (b) ring-2 with 3C(b) type of channel configuration as an example. (c) Mutual information between two rings with transfer pathways of 1C ∼ 3C configurations. (d) Exciton population in ring-2 for the 2-ring systems with transfer pathways of 1C ∼ 3C configurations. Note that for 1C and 3C configurations, only a few selected configurations have been included.

Gaussian distribution (standard deviation $\delta = 0.3\omega_0$) in our model. This is a reasonable assumption considering that the protein or solution environment induces stochastic effects in a realistic LH2 system.[48] The real space dynamics of exciton probability with 3C(b) type of channel configuration in ring-1 and ring-2 is plotted in Figs. 6(a) and 6(b), respectively. The results have been averaged over 100 realizations. Visible from Fig. 6 is the propagation of the delocalized exciton in ring-1 and its subsequent transfer to ring-2 despite the inclusion of static disorder. Interestingly, apart from the diffused pathways of exciton transfer in ring-1, there also emerge additional sharp pathways in Fig. 6(a). Furthermore, such features in the excitonic evolution appear to regularly crossover at an interval of nearly 5 phonon periods. Those sharp pathways are attributed to the exciton-phonon interaction, representing the effect of phonon wave packets motion on the evolution of the exciton population. However, such features are absent in ring-2 as the exciton population within it is rather small.

Quantum coherence, anticipated to play a major role in EET processes, introduces correlations among wave function amplitudes at different sites in the LH2 rings. Therefore, we invoke the "mutual information," a powerful tool to study coherence or correlation between two subsystems, defined as

$$I_{AB} = S_A + S_B - S_{AB}, \tag{7}$$

where $S_X = -\sum_i \lambda_i \log_2 \lambda_i$ represents the von Neumann entropy of the reduced density matrix ρ_X of subsystem X evaluated in terms of its eigenvalues $\{\lambda_i\}$.[47] Here ρ_X is written as

$$\rho_X(t) = \mathrm{Tr}\left[\rho(t)\hat{a}_m^{X\dagger}\hat{a}_n^X\right], \quad m \text{ and } n \in X, \tag{8}$$

where $\rho(t) = \left|\Phi_{D_1}(t)\right\rangle\left\langle\Phi_{D_1}(t)\right|$ is the full density matrix at zero temperature, and $|\Phi_{D_1}(t)\rangle$ is total wave-function of our model. For the detailed derivation, the reader is referred to Eq. (A16) in the Appendix. Eq. (7) can be directly used to analyze quantum coherence and quantum correlation caused by the transfer channels between LH2 rings. To facilitate further discussion, the mutual information I_{AB} and the population of ring-2 are plotted in Figs. 6(c) and 6(d), respectively. It is found that the two quantities show almost similar trends indicating a direct mapping between them. A higher degree of inter-ring coherence or correlations can indeed lead to more efficient energy transfer, consistent with recent experimental

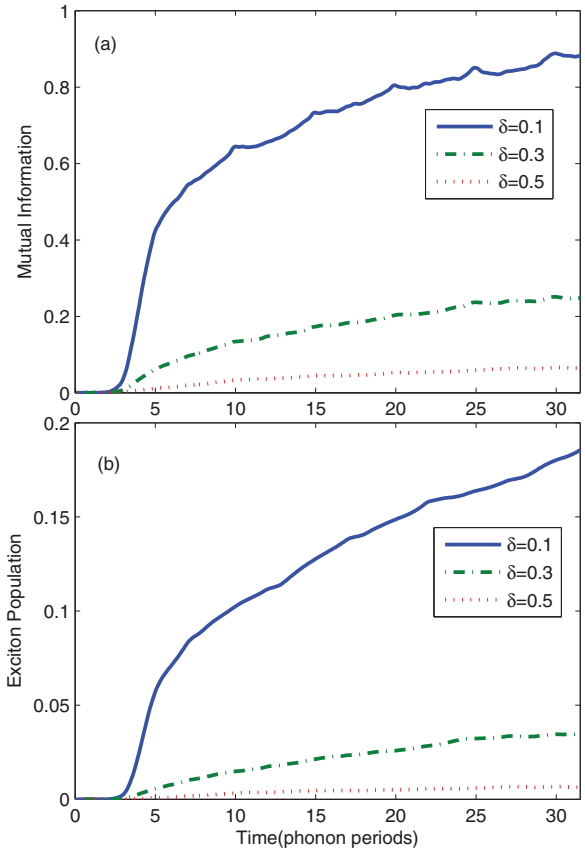

FIG. 7. Effect of the static disorder strength δ on (a) the mutual information between two rings with transfer pathways of 3C(b) type, and (b) the real space dynamics of exciton probability $|\alpha_n(t)|^2$ in ring-2 with 3C(b) type pathways. The parameters are the same as in Fig. 6 except that a distance 20 Å between the two rings is taken.

and theoretical results.[20,32,49] Meanwhile, some small peaks with a spacing of about 5 phonon periods are visible in Fig. 6(c), indicating that the phonon-motion features may be reflected in the mutual information. The spacing of the small peaks is determined by the group velocity of the phonon wave packets, which is proportional to the phonon bandwidth.[41] Compared to the population dynamics, the mutual information seems to exhibit much richer dynamics.

In Fig. 7, we plot as a function of time the mutual information between the two rings and the exciton population in ring-2 with 3C(b) type at three representative strengths of static disorder ($\delta = 0.1\omega_0$, $0.3\omega_0$, and $0.5\omega_0$). While the aforementioned small peaks are present in the mutual information plot at relatively weak static disorder ($\delta = 0.1\omega_0$), they are largely quenched in the exciton population plot. With an increasing static disorder strength, the mutual information and the exciton population are found to decrease accompanied with the disappearance of the small peaks, due to the formation of localization. It is expected that excessive static disorder would induce totally localized exciton states. It is thus the intricate interplay between quantum coherence and environment induced disorder that contribute to the overall highly efficient energy transfer in the LH2 ring system.

IV. CONCLUSIONS

In this paper, we have investigated the energy transfer induced by different pathways in a dual-ring LH2 complexes arrangement. The D_1 Ansatz time-dependent variational method is employed to study the intra- and inter-ring exciton dynamics. For simplicity, only the nearest-neighbor couplings for the cases of $J_1 = J_2$ and $J_1 \neq J_2$ are considered. We observe that the dynamical behavior of exciton is influenced by constructive or destructive interference phenomenon induced by different transfer pathways. Dimerization ($J_1 \neq J_2$) in the LH2 ring is revealed to be a major factor underlying the intra-ring quantum interference, and the exciton tends to exhibit localized characteristics within a certain dimer block. We have further found that dimerization can improve the average efficiency of the population transfer during the first 10 phonon periods. In the presence of static disorder, we have used the mutual information to study the coherence or correlation between two rings. Quantum coherence between the rings boosts the population transfer. In addition, the regular small peaks in the mutual information curves reflect the phonon motion process, which embodies the coupling between the phonons and the exciton. Interesting sharp features that overlap periodically are observed in the evolution of exciton probability, which are attributed to the exciton-phonon interactions, and are found to be dependent upon the exciton population. The crossover period is found to be consistent with the peaks in the mutual information curves as well. While a macroscopic number of low-frequency environmental modes, which introduce decoherence, play an important role in the energy transfer process, in this work we mainly focus on path-induced coherent energy transfer between two LH2 rings. In brief, we establish that the exciton dynamics is generally affected by two major factors, viz., interference effects and static disorder, which ultimately determine the efficiency of the EET processes.

ACKNOWLEDGMENTS

Support from the Singapore National Research Foundation through the Competitive Research Programme (CRP) under Project No. NRF-CRP5-2009-04 is gratefully acknowledged. One of us (K.W.S.), supported also in part by the Zhejiang Provincial Education Department Project No. Y201223209, thanks Prathamesh Shenai for helpful discussion.

APPENDIX: DETAILED DERIVATION OF EXCITON DYNAMICS IN MULTIPLE-RING SYSTEM

The D_1 trial state can be written in a general form as

$$|\Psi_{D_1}(t)\rangle = \sum_{r,n} \alpha_n^r(t)\hat{a}_n^{r\dagger}\hat{U}_n^{r\dagger}(t)|0\rangle_{\rm ex}|0\rangle_{\rm ph}, \tag{A1}$$

where $\alpha_n^r(t)$ are the variational parameters representing exciton amplitudes, and $\hat{U}_n^{r\dagger}(t)$ is the Glauber coherent operator

$$\hat{U}_n^{r\dagger}(t) \equiv \exp\left\{\sum_q \left[\lambda_{n,q}^r(t)\hat{b}_q^{r\dagger} - \text{H.c.}\right]\right\}. \tag{A2}$$

System energies of the multiple-ring system can be obtained as follows by applying the Davydov Ansätze to the modified Holstein Hamiltonian given in Eqs. (2), (3), and (4):

$$E_{\rm ex}(t) = \sum_{r_1 r_2} \sum_{nm} J_{nm}^{r_1 r_2} \alpha_n^{r_1 *}(t) \alpha_m^{r_2}(t) S_{nm}^{r_1 r_2}(t), \tag{A3}$$

$$E_{\rm ph}(t) = \sum_{r} \sum_{n} \left|\alpha_n^r(t)\right|^2 \sum_{q} \omega_q^r \left|\lambda_{nq}^r(t)\right|^2, \tag{A4}$$

$$E_{\rm ex-ph}(t) = -\frac{2}{\sqrt{N}} \sum_{r} \sum_{n} \sum_{q} g_q^r \omega_q^r \left|\alpha_n^r(t)\right|^2 {\rm Re}\left[e^{iqn} \lambda_{nq}^r(t)\right], \tag{A5}$$

with the Debye-Waller factor $S_{nm}^{r_1 r_2}(t)$ given by

$$S_{nm}^{r_1 r_2}(t) = \exp\left\{\sum_q \left[\lambda_{nq}^{r_1 *}(t) \lambda_{mq}^{r_2}(t) \delta_{r_1 r_2} - \frac{1}{2}\left|\lambda_{nq}^{r_1}(t)\right|^2 - \frac{1}{2}\left|\lambda_{mq}^{r_2}(t)\right|^2\right]\right\}, \tag{A6}$$

and the indices r_1 and r_2 run over 1 to $N_{\rm ring}$. A linear phonon dispersion with $\omega_q^r = \omega_0[1 + W(2|q|/\pi - 1)]$ is adopted, where W is a constant between 0 and 1, and the band width of the phonon frequency is $2W\omega_0$.

The approach we adopt in this work is the Lagrangian formalism of the Dirac–Frenkel time-dependent variational method,[46] a powerful technique to obtain approximate dynamics of many-body quantum systems for which exact solutions often elude researchers. We formulate the Lagrangian L as follows:

$$L = \langle \Phi(t)| \frac{i\hbar}{2} \left(\frac{\overrightarrow{\partial}}{\partial t} - \frac{\overleftarrow{\partial}}{\partial t}\right) - \hat{H} |\Phi(t)\rangle. \tag{A7}$$

From this Lagrangian, equations of motion for the M functions of time, parameters $\alpha_m^r(t)$, and their time-derivatives $\dot{\alpha}_m^r(t)$ $(m = 1, \ldots, M)$, can be obtained by

$$\frac{d}{dt}\left(\frac{\partial L}{\partial \dot{\alpha}_m^{r*}}\right) - \frac{\partial L}{\partial \alpha_m^{r*}} = 0. \tag{A8}$$

Therefore, the equations of motions for the time-dependent variational parameters $\alpha_n^r(t)$ and $\lambda_{nq}^r(t)$ are written as

$$\dot{\alpha}_n^r(t) = i\left[T_n^r(t) + \alpha_n^r(t) R_n^r(t)\right], \tag{A9}$$

and

$$\dot{\lambda}_{nq}^r(t) = i\left[\frac{\Omega_{nq}^r(t)}{\alpha_n^r(t)} + \frac{g_q^r}{\sqrt{N}} \omega_q^r e^{-iqn} - \omega_q^r \lambda_{nq}^r(t)\right]. \tag{A10}$$

Each collected term in Eqs. (A9) and (A10) is given as

$$\varpi_{nq}^r(t) = i\dot{\lambda}_{nq}^r(t) + \frac{g_q^r}{\sqrt{N}} \omega_q^r e^{-iqn} - \omega_q^r \lambda_{nq}^r(t), \tag{A11}$$

$$R_n^r(t) = Re \sum_q \left[\varpi_{nq}^r(t) + \frac{g_q^r}{\sqrt{N}} \omega_q^r e^{-iqn}\right] \lambda_{nq}^{r*}(t), \tag{A12}$$

$$T_n^{r_1}(t) = -\sum_{r_2} \sum_{m} J_{nm}^{r_1 r_2} \alpha_m^{r_2}(t) S_{nm}^{r_1 r_2}(t), \tag{A13}$$

$$\Omega_{nq}^{r_1}(t) = -\sum_{r_2} \sum_{m} J_{nm}^{r_1 r_2} \alpha_m^{r_2}(t) S_{nm}^{r_1 r_2}(t)\left[\lambda_{mq}^{r_2}(t) \delta_{r_1 r_2} - \lambda_{nq}^{r_1}(t)\right], \tag{A14}$$

After solving the coupled equations of motion, the reduced single-exciton density matrix $\rho_{mn}^{r_1 r_2}(t)$ can be obtained from

$$\rho_{mn}^{r_1 r_2}(t) = {\rm Tr}\left[\rho(t) \hat{a}_m^{r_1 \dagger} \hat{a}_n^{r_2}\right], \tag{A15}$$

where $\rho(t) = |\Phi(t)\rangle\langle\Phi(t)|$ is the full density matrix at zero temperature, and $|\Phi(t)\rangle$ is the total polaron wave function at time t after the photoexcitation takes place. Substituting the detailed form of the D_1 Ansatz into the polaron wave function, one obtains

$$\rho_{mn}^{r_1 r_2}(t) = \langle \Psi_{D_1}(t)| \hat{a}_m^{r_1 \dagger} \hat{a}_n^{r_2} |\Psi_{D_1}(t)\rangle = \alpha_m^{r_1 *}(t) \alpha_n^{r_2}(t) S_{mn}^{r_1 r_2}(t). \tag{A16}$$

[1] G. McDermontt, S. M. Prince, A. A. Freer, A. M. Hawthornthwaite, M. Z. Papiz, R. J. Cogdell, and N. W. Issacs, Nature (London) **374**, 517 (1995).
[2] J. Koepke, X. Hu, C. Muenke, K. Schulten, and H. Michel, Structure **4**, 581 (1996).
[3] Y. Zhao, M. F. Ng, and G. H. Chen, Phys. Rev. E **69**, 032902 (2004).
[4] K. Sauer, Annu. Rev. Phys. Chem. **30**, 155 (1979).
[5] R. E. Blankenship, *Molecular Mechanisms of Photosynthesis* (Blackwell Science, Oxford/Malden, 2002).
[6] R. van Grondelle and V. I. Novoderezhkin, Phys. Chem. Chem. Phys. **8**, 793 (2006).
[7] G. S. Engel, T. R. Calhoun, E. L. Read, T. K. Ahn, T. Mancal, Y. C. Cheng, R. E. Blankenship, and G. R. Fleming, Nature (London) **446**, 782 (2007).
[8] E. Collini, C. Y. Wong, K. E. Wilk, P. M. Curmi, P. Brumer, and G. D. Scholes, Nature (London) **463**, 644 (2010).
[9] G. Panitchayangkoon, D. Hayes, K. A. Fransted, J. R. Caram, E. Harel, J. Wen, R. E. Blankenship, and G. S. Engel, Proc. Natl. Acad. Sci. U.S.A. **107**, 12766 (2010).
[10] E. Collini *et al.*, Science **323**, 369 (2009).
[11] T. R. Calhoun and G. R. Fleming, Phys. Status Solidi B **248**, 833 (2011); T. D. Huynh, K. W. Sun, M. Gelin, and Y. Zhao, J. Chem. Phys. **139**, 104103 (2013).
[12] R. Hildner, D. Brinks, J. B. Nieder, R. J. Cogdell, and N. F. van Hulst, Science **340**, 1448 (2013).
[13] L. P. Chen, M. Gelin, W. Domcke, and Y. Zhao, "Polaron dynamics in femtosecond single-molecule spectroscopy of light harvesting systems," J. Phys. Chem. A (submitted).
[14] T. Brixner, J. Stenger, H. M. Vaswani, M. Cho, R. E. Blankenship, and G. R. Fleming, Nature (London) **434**, 625 (2005).
[15] A. Olaya-castro, C. F. Lee, F. F. Olsen, and N. F. Johnson, Phys. Rev. B **78**, 085115 (2008).
[16] F. Fassioli, A. Olaya-castro, S. Scheuring, J. N. Sturgis, and N. F. Johnson, Biophys. J. **97**, 2464 (2009).
[17] F. Müh, M. EI-A. Madjet, J. Adolphs, A. Abdurahman, B. Rabenstein, H. Ishikita, E. W. Knapp, and T. Renger, Proc. Natl. Acad. Sci. U.S.A. **104**, 16862 (2007).
[18] S. Jang, M. D. Newton, and R. J. Silbey, Phys. Rev. Lett. **92**, 218301 (2004).
[19] S.-H. Yeh, J. Zhu, and S. Kais, J. Chem. Phys. **137**, 084110 (2012).
[20] A. Ishizaki and G. R. Fleming, Proc. Natl. Acad. Sci. U.S.A. **106**, 17255 (2009).
[21] J. S. Cao and R. J. Silbey, J. Phys. Chem. A **113**, 13825 (2009).
[22] J. H. Kim and J. S. Cao, J. Phys. Chem. B **114**, 16189 (2010).
[23] J. S. Cao and R. J. Silbey, J. Phys. Chem. **112**, 12867 (2008).
[24] J. Zhu, S. Kais, P. Rebentrost, and A. Aspuru-Guzik, J. Phys. Chem. B **115**, 1531 (2011).
[25] M. Mohseni, P. Rebentrost, S. Lloyd, and A. Aspuru-Guzik, J. Chem. Phys. **129**, 174106 (2008).
[26] M. B. Plenio and S. F. Huelga, New J. Phys. **10**, 113019 (2008).
[27] P. Rebentrost, M. Mohseni, I. Kassal, S. Lloyd, and A. Aspuru-Guzik, New J. Phys. **11**, 033003 (2009).
[28] A. Olaya-Castro, C. F. Lee, F. Fassioli Olsen, and N. F. Johnson, Phys. Rev. B **78**, 085115 (2008).
[29] F. Caruso, A. W. Chin, A. Datta, S. F. Huelga, and M. B. Plenio, J. Chem. Phys. **131**, 105106 (2009); Phys. Rev. A **81**, 062346 (2010).
[30] A. W. Chin, A. Datta, F. Caruso, S. F. Huelga, and M. B. Plenio, New J. Phys. **12**, 065002 (2010).

[31]P. Giorda, S. Garnerone, P. Zanardi, and S. Lloyd, "Interplay between coherence and decoherence in LHCII photosynthetic complex," preprint arXiv:1106.1986v1 (2011).
[32]G. D. Scholes, G. R. Fleming, A. O. Castro, and R. V. Grondelle, Nat. Chem. **3**, 763 (2011).
[33]H. P. Breuer and F. Petruccione, *The Theory of Open Quantum Systems* (Oxford University Press, Oxford, 2002).
[34]A. G. Redfield, IBM J. Res. Dev. **1**, 19 (1957).
[35]D. J. Heijs, V. A. Malyshev, and J. Knoester, Phys. Rev. Lett. **95**, 177402 (2005).
[36]M. Schröder, U. Kleinekathofer, and M. Schreiber, J. Chem. Phys. **124**, 084903 (2006).
[37]G. D. Scholes, Annu. Rev. Phys. Chem. **54**, 57 (2003).
[38]Y. C. Cheng and G. R. Fleming, Annu. Rev. Phys. Chem. **60**, 241 (2009).
[39]B. Luo, J. Ye, C. B. Guan, and Y. Zhao, Phys. Chem. Chem. Phys. **12**, 15073 (2010).
[40]B. Luo, J. Ye, and Y. Zhao, Phys. Status Solidi C **8**, 70 (2011).
[41]J. Sun, B. Luo, and Y. Zhao, Phys. Rev. B **82**, 014305 (2010); Y. Zhao, P. Zanardi, and G. Chen, Phys. Rev. B **70**, 195113 (2004).
[42]T. Holstein, Ann. Phys. **8**, 325 (1959); **8**, 343 (1959).
[43]G. D. Mahan, *Many Particle Physics*, 3rd ed. (Kluwer Academic, 2000).
[44]X. Hu, T. Ritz, A. Damjanović, and K. Schulten, J. Phys. Chem. B **101**, 3854 (1997).
[45]A. Damjanović, I. Kosztin, U. Kleinekathöer, and K. Schulten, Phys. Rev. E **65**, 031919 (2002).
[46]C. Itzykson and J. Zuber, *Many-Particle Physics* (McGraw-Hill, New York, 1980).
[47]M. A. Nielsen and I. L. Chuang, *Quantum Computation and Quantum Information* (Cambridge University Press, Cambridge, 2000).
[48]V. Butkus, A. Gelzinis, and L. Valkunas, J. Phys. Chem. A **115**, 3876–3885 (2011).
[49]G. S. Schlau-Cohen, A. Ishizaki, T. R. Calhoun, N. S. Ginsberg, M. Ballottari, R. Bassi, and G. R. Fleming, Nat. Chem. **4**, 389 (2012).